Solar center-to-limb variation in Rossiter-McLaughlin and exoplanet transmission spectroscopy

A. Reiners[1], F. Yan[2], M. Ellwarth[1], H.-G. Ludwig[3], and L. Nortmann[1]

[1] Institut für Astrophysik und Geophysik, Georg-August-Universität, D-37077 Göttingen, Germany
[2] Department of Astronomy, University of Science and Technology of China, Hefei 230026, China
[3] Landessternwarte, Zentrum für Astronomie der Universität Heidelberg, D-69117 Heidelberg, Germany

ABSTRACT

Line profiles from spatially unresolved stellar observations consist of a superposition of local line profiles that result from observing the stellar atmosphere under specific viewing angles. Line profile variability caused by stellar magnetic activity or planetary transit selectively varies the weight and/or shape of profiles at individual surface positions. The effect is usually modeled with radiative transfer calculations because observations of spatially resolved stellar surfaces are not available. For the Sun, we recently obtained a broadband spectroscopic atlas of the solar center-to-limb variation (CLV). We use the atlas to study systematic differences between largely used radiative transfer calculations and solar observations. We concentrate on four strong lines useful for exoplanet transmission analysis, and we investigate the impact of CLV on transmission and Rossiter-McLaughlin (RM) curves. Solar models used to calculate synthetic spectra tend to underestimate line core depths but overestimate the effect of CLV. Our study shows that CLV can lead to significant systematic offsets in transmission curves and particularly in RM curves; transmission curves centered on individual lines are overestimated by up to a factor of two by the models, and simulations of RM curves yield amplitudes that are off by up to 5–10 m s^{-1} depending on the line. For the interpretation of transit observations, it is crucial for model spectra that accurately reproduce the solar CLV to become available which, for now, is the only calibration point available.

Key words. keywords

1. Introduction

The solar spectrum varies across the visible surface because of limb darkening caused by temperature stratification of the solar atmosphere, and because the opacity distribution and non-local thermodynamic equilibrium (non-LTE) effects differ between spectral lines (see, e.g., Stenflo 2015). The projected convective velocity distribution depends on the formation height and angle of projection. Limb darkening and its wavelength variability provide observable constraints for the structure of the Sun's atmosphere (Asplund et al. 2009) which, until today, have only partially been exploited. One reason for this is the lack of observations at different values of center-to-limb distance, parameterized by $\mu = \cos \theta$ with the heliocentric angle θ. Ellwarth et al. (2023) recently presented a spectral library of solar center-to-limb variation (CLV).

The Sun serves as a benchmark for other stars. Doppler radial velocity (RV) measurements and transit spectroscopy critically depend on differential comparison between stellar reference or template spectra, and spectroscopic data taken at different times. Most stars other than the Sun cannot be spatially resolved, and assumptions about their limb darkening and variability are motivated by the solar example. An important task for improving RV measurement precision is understanding how RV variability is driven by convection and its interplay with magnetic fields (Lagrange et al. 2010; Lanza et al. 2010; Meunier et al. 2010a,b; Dumusque et al. 2014; Marchwinski et al. 2015; Haywood et al. 2016; Milbourne et al. 2019). The motion of hot, rising plasma on the surface of a star causes a Doppler shift of the observed spectrum (Beckers & Nelson 1978; Dravins et al. 1981;

Livingston 1982). Because the motion of the plasma is non-isotropic, the amplitude of the Doppler shift varies across the stellar disk, which means it depends on the stellar limb position, and can be visualized spectroscopically (Balthasar 1984; Cavallini et al. 1985). For a Sun-like star, the disk-integrated effect is on the order of a hundred m s^{-1} such that the observed RV of a star is systematically blueshifted (see, e.g., Nordlund et al. 2009).

Atmospheres of extrasolar planets can be studied during planetary transits when the light of the star penetrates the planetary atmosphere. For this, the background stellar spectrum must be known to very high precision, and the contribution from the part of the surface occulted during transit needs to be carefully considered. Knowledge about the nonuniformity of the stellar flux across the stellar disk is crucial for this technique (Czesla et al. 2015; Yan et al. 2017). Differential limb darkening affects the influence of the transiting planet on the spectrum and is a major source of uncertainty for transit spectroscopy (Csizmadia et al. 2013; Espinoza & Jordán 2015; Parviainen & Aigrain 2015; Maxted & Gill 2019). Furthermore, the stellar lines have very different shapes across the stellar surface (the effect of CLV; Athay et al. 1972; Dravins et al. 1981; Balthasar 1984; Yan et al. 2015). Recently, the presence of Na I and other absorbing species in the atmosphere of HD 209458b was questioned by transit observations with different instruments (Casasayas-Barris et al. 2020, 2021). Features around the stellar Na I lines observed during transit could be interpreted as signatures of the deformation of the stellar line profiles, due to the Rossiter-McLaughlin (RM) effect and CLV. The signature is very similar to the one from exoplanet atmosphere absorption.

Chiavassa & Brogi (2019) demonstrate that considering limb darkening and CLV significantly improves planet detectability from transit spectroscopy. This, however, must go together with improving our understanding of stellar magnetoconvection. Unfortunately, no suitable observations of spatially resolved stellar surfaces are available against which the model line profiles across the stellar disk could be calibrated. In this context, Dravins et al. (2017a) point out the importance of testing 3D and time-dependent hydrodynamic models, as the one used in this work, against observations, and Dravins et al. (2021) discuss the prospects for obtaining spatially resolved stellar spectroscopy from transit observations. Dravins et al. (2017b) attempted to extract local line profiles from transit observations of HD 209458, and solar eclipse observations by Reiners et al. (2016a) demonstrate the same conceptual difference between a model and observations. An improvement in quality is expected for observations in stars other than the Sun when observations with 30 m-class telescopes become available. Until then, the Sun is the only star for which spatially resolved spectroscopy at the required spectral fidelity is feasible.

We recently obtained a new grid of the spectrally resolved solar CLV (Ellwarth et al. 2023). In this paper, we select four spectral lines and demonstrate data quality and line profile variations at different limb positions. We compare the lines to models of line profiles from simulations that are frequently used for the modeling of RV variability and transit observations, and we estimate the impact on transmission curves and the RM effect.

2. Data

We compare observations of the solar CLV with three sets of model spectra. All datasets are accessible online.[1]

2.1. Observations

Our observations of the Sun at different limb positions, $\mu = \cos\theta$, are described in detail in Ellwarth et al. (2023). We obtained spectra at 14 different limb positions of which we use the following 12 for this paper: $\mu = 0.2, 0.3, 0.4, 0.5, 0.6, 0.7, 0.8, 0.9, .95, 0.98, 0.99$, and 1.0. With respect to the available 14 positions, we chose to neglect two at $\mu = 0.35$ and 0.97 to achieve a more regular sampling. The Sun was observed with the 50 cm Vacuum Vertical Telescope at the Institute for Astrophysics and Geophysics, Göttingen (Schäfer et al. 2020b). Spectra were obtained with our Fourier Transform Spectrometer (FTS; Schäfer et al. 2020a) in the range $\lambda = 4200 - 8000$ Å at a resolving power $R = 700\,000$ at $\lambda = 6000$ Å ($\Delta \nu = 0.0024\,\mathrm{cm}^{-1}$). Each observation covers the entire wavelength range providing superior wavelength (frequency) calibration (see Reiners et al. 2016b). We estimate that the linearity of the wavelength calibration is better than $0.5\,\mathrm{m\,s}^{-1}$ at all wavelengths (Huke et al. 2019) and that the uncertainty of the absolute zero point offset of each spectrum is below $30\,\mathrm{m\,s}^{-1}$ (Ellwarth et al. 2023).

The CLV atlas was not corrected for gravitational redshift. We applied a Doppler shift of $\Delta \nu = -633.1\,\mathrm{m\,s}^{-1}$ (González Hernández et al. 2020) for the comparison with model spectra.

Table 1. Parameters of the synthetic calculations.

	SME LTE	SME NLTE	CO^{5}BOLD
LTE/NLTE	LTE	NLTE	LTE
1D/3D		1D	3D
T_{eff} (K)		5800	5774
$\log g$		4.45	4.44
λ range (Å)		4700 – 7900	1200 – 10000
μ values		[0.2, 0.3, 0.4, ..., 0.9, 0.95, 0.98, 0.99, 1.0]	[0.09, 0.41, 0.79, 1.0]
sampling ($\Delta \nu$)		130 m s^{-1}	330 m s^{-1}

2.2. Synthetic spectra

In the following, we compare our observations to three sets of synthetic spectra to demonstrate typical model predictions about CLV. Our goal is to identify the typical systematic differences between models and the solar spectrum. We concentrate on "standard" models that are commonly used in stellar line profile analysis and exoplanet transmission spectroscopy. We do not attempt to provide the best match possible but calculate the model spectra with parameters according to a "typical" main sequence Sun-like star.

Two of the fundamental choices in computations of spectral line formation are the treatment of local thermodynamic equilibrium (LTE) and of convection. We computed 1D models for the assumption of LTE and with corrections for NLTE, and we computed spectra with a 3D convection model under the assumption of LTE. We leave computations of 3D convection together with NLTE and optimization of any parameters for in-depth studies of atmospheric models. An overview of the model parameters is provided in Table 1. As for the expected differences between the 1D and 3D approach, and the difference between LTE and NLTE spectral line formation, we refer to Nordlund et al. (2009) and Asplund et al. (2009) and the SME references (see below).

2.2.1. SME

One-dimensional models in LTE and NLTE were computed with the software package Spectroscopy Made Easy (SME; Valenti & Piskunov 1996; Piskunov & Valenti 2017)[2] with atomic and molecular line data from VALD3 (Piskunov et al. 1995; Kupka et al. 1999) and MARCS atmospheric models (Gustafsson et al. 2008). For effective temperature and surface gravity, we chose $T_{\mathrm{eff}} = 5800\,\mathrm{K}$ and $\log g = 4.45$, and solar abundances are adopted from Grevesse et al. (2007, see Appendix A). Microturbulence was set to $v_{\mathrm{mic}} = 1\,\mathrm{km\,s}^{-1}$, and macroturbulence was set to zero. Departure coefficients for NLTE calculations were taken from Amarsi et al. (2016) for Fe and from Amarsi et al. (2020) for Ca, K, Mg, Na, and O. We computed a grid of models for the same μ values as our observations.

2.2.2. CO^{5}BOLD

A synthetic LTE spectrum was calculated with the ASSϵT code (Koesterke et al. 2008; Koesterke 2009) for a 3D and time-dependent solar model atmosphere calculated with the CO^{5}BOLD code (Freytag et al. 2012). The code explicitly includes and resolves convective motions in the atmosphere.

---

[1] http://www.astro.physik.uni-goettingen.de/research/solar-clv

[2] https://www.stsci.edu/~valenti/sme.html

Hydrodynamical simulations of the stellar convection code with CO^{5}BOLD solve the equations for the compressible hydrodynamics coupled with non-local transport of radiation with detailed opacities. The line spectral line list from the TLUSTY/SYNSPEC code was used (Hubeny & Lanz 2011). The particular CO^{5}BOLD model was previously applied in projects aiming to determine several elemental abundances in the solar photosphere (Caffau et al. 2011; Steffen et al. 2015), and it is a member of the CIFIST grid of 3D model atmospheres (Ludwig et al. 2009; Tremblay et al. 2013). In brief, the computational domain has a size of $5.6 \times 5.6 \times 2.25 \,\mathrm{Mm}^3$ covered by $140 \times 140 \times 150$ mesh points. The temporal evolution over 2.1 h was represented by 20 statistically independent instances in time. To reduce computational cost, the model was horizontally subsampled by a factor of three. The final spectra for the various limb positions are averages of the emergent intensity over time and horizontal position. Appendix A lists the abundances that were assumed in the spectral synthesis with ASSϵT. We emphasize that no effort was made to fit particular lines or spectral regions.

Synthetic CO^{5}BOLD spectra are available for limb positions $\mu = 0.09, 0.41, 0.79, 1.0$. For comparison to observations, we interpolated the CO^{5}BOLD spectra to the observed μ grid. We applied 2D cubic convolution interpolation (λ, μ) based on the triangulation algorithm from Lee & Schachter (1980).

3. Center-to-limb variation

The full spectral library and all model spectra are available online. Users can inspect CLV in all spectral lines contained in the wavelength range and compare the three different models to observations. Here, we show four lines as typical examples of CLV and discuss the influence of NLTE and 3D convection on the spectral lines, and compare them to our observations. In Fig. 1, we show spectral lines of Na I, Mg I, Ca I, and Fe I from top to bottom. Each panel shows the observed FTS data for five limb positions $\mu = 0.2, 0.4, 0.6, 0.8,$ and 1.0. From left to right, we overplotted the three sets of model spectra, SME LTE, SME NLTE, and CO^{5}BOLD (LTE and 3D convection). In Fig. 2, we show the ratio between spectra from different limb positions and spectra at disk center for the observations and models for the same four lines, that is, in this figure the lines for $\mu = 1$ are constant at ratio 1. We discuss trends for the observations and models in the following.

3.1. IAG FTS observations

The observed IAG FTS data are shown as solid lines in Fig. 1, values of μ are color-coded, and black lines show $\mu = 1$. The spectra for individual limb positions are averages observed across the solar disk that are corrected for solar rotation. The spectral lines' maximum absorption exceeds 80 % at line center in all four lines. The left panel in Fig. 2 shows the ratios between IAG FTS observations with respect to disk center.

The **Na I line** (top panel in Figs. 1 and 2) shows a relatively broad line center and steep flanks around the core. Damping wings are less steep. The line core remains relatively constant for different μ values, and the damping wings show a discernable CLV of approximately 5 % absorption depth between μ values with $\Delta\mu = 0.2$. Ratios in Fig. 2 show that the line asymmetry shifts from the disk center to limb. We note that we use the Na I line centered at $\lambda = 5897.6\,\text{Å}$. We show the line only in a range $\Delta v = \pm 20\,\mathrm{km\,s^{-1}}$ around the line center. This is because

of a telluric line that is located in the right wing of the line. The Na I at $5891.6\,\text{Å}$ (not shown in this work) is even more severely contaminated by telluric lines. For the Mg I line, we show the range within $\Delta v = \pm 40\,\mathrm{km\,s^{-1}}$, and for Ca I and Fe I, we show $\Delta v = \pm 30\,\mathrm{km\,s^{-1}}$. For this work, we did not attempt any telluric correction of the IAG FTS spectra. The wavelength ranges selected show little impact of telluric contamination such that a correction would not significantly alter the results.

The **Mg I line** (second panel) is similar in shape to the Na I line, but the center is more curved and the damping wings are stronger. The CLV follows a similar trend with little variation in the core but significantly weaker absorption closer to the solar limb in the wings. The latter is more clearly visible than in the Na I lines because the damping wings appear less steep and lines from different limb positions appear more clearly separated. The line symmetry is relatively constant across the disk, which can be seen in the line ratios in Fig. 2.

The **Ca I line** (third panel) and also the **Fe I line** (bottom panel) show smooth Voigt profiles. The CLV in both lines is relatively weak. Lines closer to the limb appear a few percent weaker than lines at disk center, but the overall shape remains largely unchanged. Line ratios in Fig. 2 reveal the shift of the line core from disk center to limb.

3.2. SME LTE

We are comparing model line profiles from SME LTE calculations to our observations in the left panel of Fig. 1. In general, the line cores in the calculations match the cores of the IAG FTS data relatively well. Toward the wings, the difference between the model and observations varies across the limb. This could be explained by convective blueshift, which is not taken into account in this model. All line cores of the model appear significantly weaker at the solar limb with respect to disk center. None of the observed lines shows CLV as strong as predicted in the SME LTE model.

The line ratio plots in the second panel of Fig. 2 reflect the overall shape of lines and the way intensity changes differently at different line depths. All patterns show the same symmetry for each line because radiative transfer in the absence of a velocity field linked with convective motions does not produce any asymmetries (Asplund et al. 2009).

3.3. SME NLTE

The line profiles from the SME NLTE calculations differ significantly from the LTE calculations in all four lines. In the Na I line, the NLTE calculations provide a reasonable match of line absorptions and CLV to the observations. This is opposite to the Mg I line for which the NLTE model predicts weaker line cores than the LTE model (but strong CLV), which means the mismatch becomes even larger. For the Ca I line, the NLTE model shows significantly weaker CLV than the LTE model. Otherwise, the difference between LTE and NLTE is relatively little in the Ca I and also in the Fe I line. As for the SME LTE case, the SME NLTE line cores match the position of the observations relatively well.

A comparison between LTE and NLTE calculations shows that among the four lines we selected, the Na I line is most sensitive to NLTE effects. In this line, the line depths in the LTE calculations are substantially smaller than in the observations, and the line depths are significantly larger in the NLTE calculations. A similar situation can be observed in the Ca I line; although, it
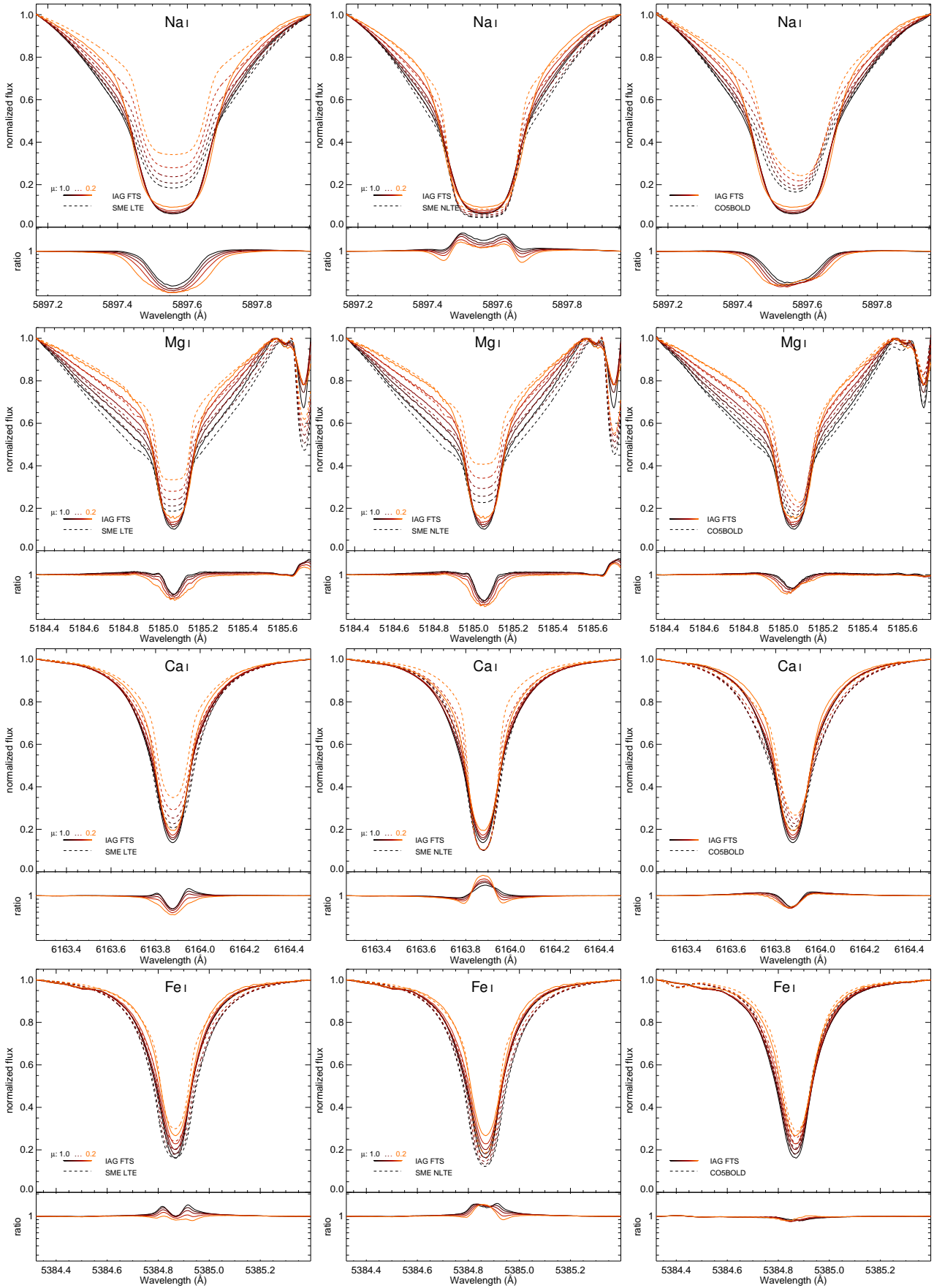
Fig. 1. Line profile comparison between observed and model spectra for four example lines Na I 5897, Mg I 5185, Ca I 6163, Fe I 5384 (top to bottom; panels span velocity ranges ±20, ±40, ±30, and ±30 km s^{-1}, respectively), and for model spectra for SME LTE, SME NLTE, and CO^{5}BOLD calculations (left to right). For each panel, the upper plot shows observed IAG FTS spectra as solid lines and model spectra as dashed lines. Lower plots show data/model ratios on a logarithmic scale. Five limb positions, $\mu = 0.2, 0.4, 0.6, 0.8, 1.0$, are shown for each set of spectra. Darker color is used for spectra taken closer to disk center.
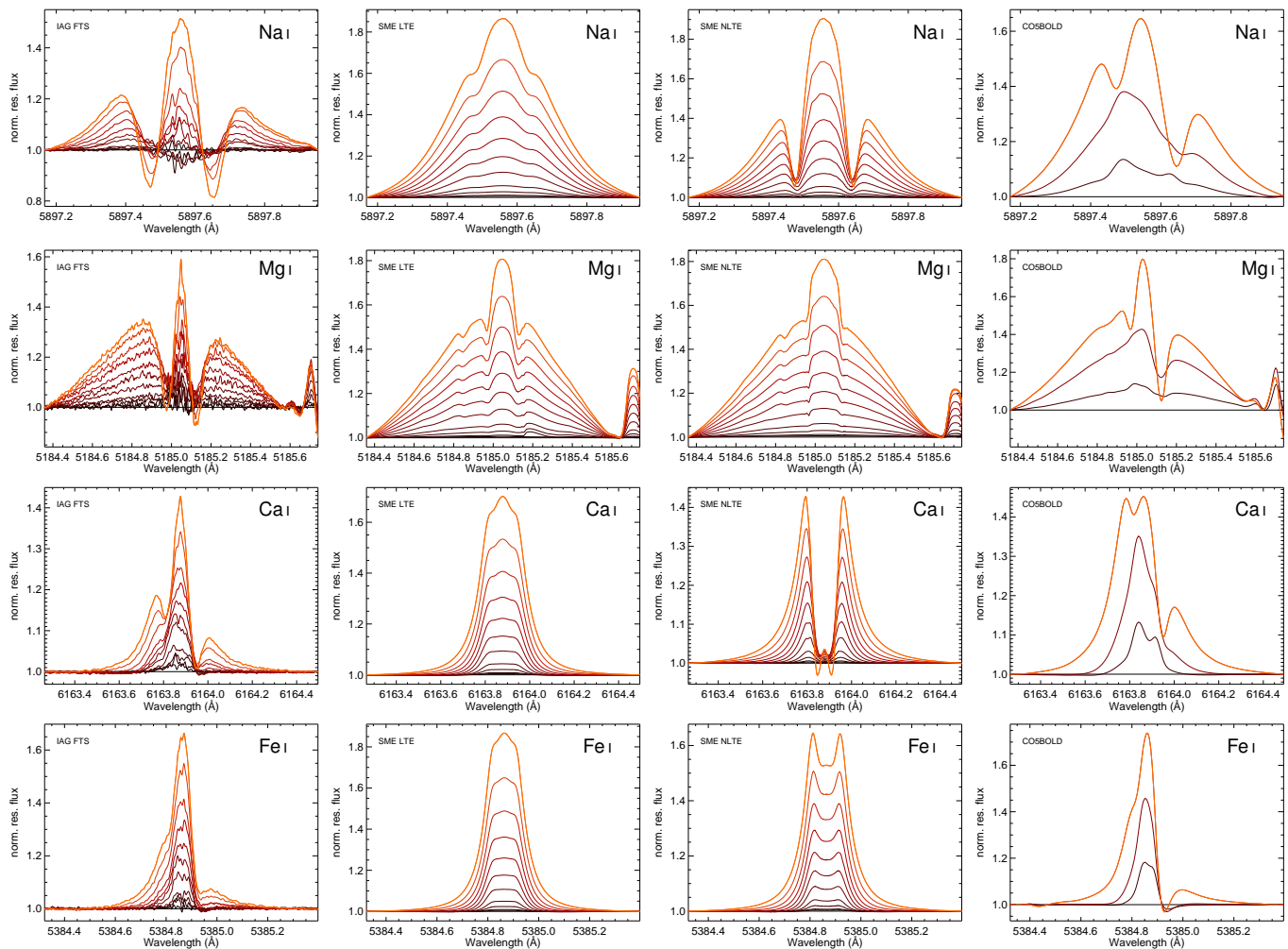
Fig. 2. Line ratios between spectra at different limb positions and the spectrum taken at disk center for four example lines: Na I 5897, Mg I 5185, Ca I 6163, and Fe I 5384 (from top to bottom, panels span velocity ranges ± 20, ± 40, ± 30, and $\pm 30\,\mathrm{km\,s^{-1}}$, respectively). The panels from left to right show observed IAG FTS spectra, and spectra for SME LTE, SME NLTE, and CO^{5}BOLD calculations as dashed lines, respectively. For IAG FTS and SME spectra, limb positions $\mu = 1.0, 0.99, 0.98, 0.95, 0.9, 0.8, 0.7, 0.6, 0.5, 0.4, 0.3, 0.2$ are shown. The CO^{5}BOLD models are available for $\mu = 1.0, 0.79, 0.41, 0.09$. A darker color is used for spectra taken closer to disk center.

is not as obvious as in Na I. In the other two lines, NLTE effects are less pronounced.

3.4. CO^{5}BOLD

The CO^{5}BOLD calculations were carried out in LTE. In general, the CLV of line strengths is similar to the SME LTE model; although, the amplitude of the variability in line strength at the core is diminished and closer to the observed behavior than SME LTE. In all four lines, the inclusion of convection in the model calculations provides some improvement against the 1D model (SME LTE). The residuals between observations and the CO^{5}BOLD spectra are particularly small for the Fe I line, while rather significant differences appear in the other lines (Fig 1). The effect of convection is clearly visible in the asymmetry of the line profile models, in particular in the blue line wings (see ratio panels in Fig 1). Including convective motion in the line formation calculations introduces an asymmetry of the line profiles that shifts the line core by several hundred m s^{-1} redward from center to limb. The effect is stronger than observed in the IAG FTS data.

In the right panel of Fig. 2, we show the line ratios from the CO^{5}BOLD calculations. In this figure, we show only calcula-

tions for which radiative transfer calculations were carried out (we avoided interpolations). The line ratios in the right panel of Fig. 2 show that the modeled profile asymmetry varies across the solar disk. This is because the projection of convective velocities toward the observer is not symmetric. It is interesting to compare the shape of ratios between the CO^{5}BOLD calculations and the IAG FTS observations. The change in line ratios predicted by the CO^{5}BOLD model shows some similarity to the observed behavior, which can be interpreted as the modeled convection partially resembling the convective velocity field on the solar surface.

4. Synthetic transit models

We used the FTS IAG atlas to simulate planetary transit observations including the effect of CLV. Furthermore, we compared our results to simulations from radiative transfer calculations with SME LTE, SME NLTE, and CO^{5}BOLD as in earlier sections, with the goal to estimate the systematics that can be expected if CLV is not taken into account. Our simulation carried out numerical integration over the visible surface of the stellar disk. The stellar surface was approximated by a grid with elements equal in size and 201 elements along the equator, which provides sufficient spatial resolution for our simulations. During transit, the elements occulted by the planet were neglected in the integration.
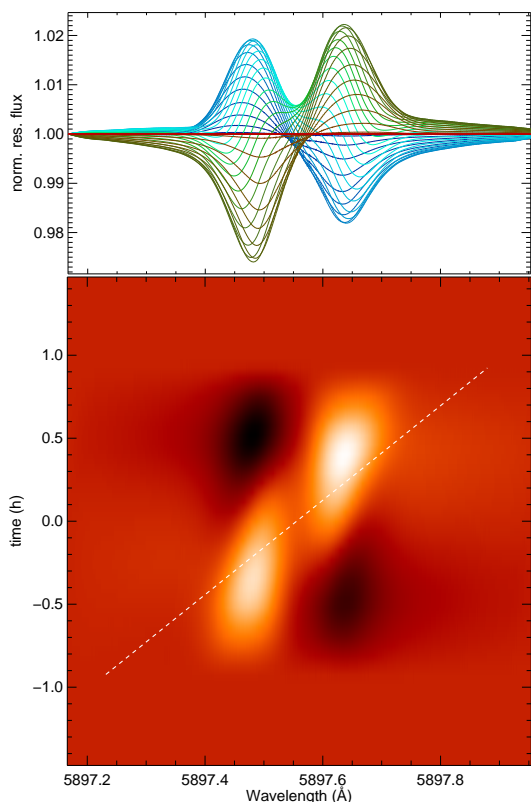
Fig. 3. Spectroscopic signature of the transiting planet in the Na I line. *Top panel:* Residuals between spectra during the transit and out-of-transit spectrum, with different colors indicating the time during transit. *Lower panel:* Residuals shown as a dynamic spectrum with color indicating normalized residual flux, and a brighter color indicating larger values. The white dashed line shows the planetary path. The plot covers a velocity range of $\pm 20\,\mathrm{km\,s^{-1}}$ around the line center.

Table 2. Configuration of planetary orbit and stellar parameters used for the transit simulations are similar to the HD 189733 system. Parameters are adopted from Triaud et al. (2009) and Yan et al. (2017).

Parameter	Value
Planet mass (M_{Jup})	1.138
Planet radius (R_{Jup})	1.505
Orbital period (d)	2.218573
Star radius ($R_{\odot}$)	0.756
Star mass ($M_{\odot}$)	0.806
Star P_{rot} (d)	12.41
Inclination of stellar rotation axis (deg)	87
Star $v \sin i$ ($\mathrm{km\,s^{-1}}$)	3.08
Eccentricity	0
Orbital inclination (deg)	85.508
Spin-orbit angle λ (deg)	-0.85
Impact parameter a	0.69

For each surface element, we interpolated the local spectrum of the FTS IAG atlas according to the element's value of μ. For the limb darkening law, we chose the tabulation of Neckel & Labs (1994) and selected the entry according to the wavelength closest to the spectral line. For each element, the spectrum was shifted according to its projected velocity toward the observer.

We demonstrate the effect of CLV for the example of a planet in orbit around a star. We use solar spectra from the IAG FTS

atlas and from solar spectrum models. For our examples, we assume a star-planet configuration similar to HD 189733b, that is, geometry and parameters of the planetary orbit resemble the HD 189733 system (see Table 2), but we use solar spectra and neither observations nor atmosphere models of HD 189733 enter our simulation. We emphasize that HD 189733 is cooler than the Sun and our local spectra are therefore not representative for this particular star. Nevertheless, our simulations provide an estimate for the order of magnitude of systematic effects that can be expected in a system similar to HD 189733.

We show an example dynamic spectrum for the Na I line in Fig. 3. The lower panel visualizes the residuals between the average out-of-transit spectrum of the star and the spectral line during transit in the range $\pm 20\,\mathrm{km\,s^{-1}}$ around line center. The radial velocity path of the planet during transit is overplotted as a dashed white line. The planetary path is similar to the spectral transit feature (the RM signature) if the planetary orbit and stellar rotation are aligned ($\lambda = 0$), and they also coincide if $P_{\mathrm{orb}} = P_{\mathrm{rot}}$. For example, the planetary path closely follows the transit feature in HD 209458 and precise correction of the RM feature is particularly important (see Casasayas-Barris et al. 2021). In the following, transmission curves are calculated in the range $\pm 20\,\mathrm{km\,s^{-1}}$ around the line center, that is, the same range as shown in Fig. 3.

4.1. Transmission curves

We show transmission curves for the four example lines in Fig. 4. The plots show the ratio between the normalized flux observed (F_{in}) and the normalized flux out of transit (F_{out}). Fluxes are normalized because absolute flux information is usually not retained in high-resolution spectroscopic observations at the level required for this measurement. This means that the transmission curve, $F_{\mathrm{in}}/F_{\mathrm{out}} - 1$, can be positive during transit even if the total flux during transit is always smaller than when out of transit. The transmission curve is negative if the spectral lines appear deeper during transit, and it is positive if the spectral lines appear shallower. The transmission curve can be computed from the dynamic spectrum (Fig. 3) by integration across the spectral domain (here, $\pm 20\,\mathrm{km\,s^{-1}}$).

The amplitude and shape of the transmission curves caused by the planetary transit in absence of any atmospheric absorption depend on the choice of the local line profiles. In all four lines, the effect is smallest if the observed FTS IAG lines are used, and the amplitudes of the transmission curves are overpredicted for all three model sets. This is a consequence of the CLV effect being overestimated in the models as seen in Fig. 1. In general, the best match is typically found for the $\mathrm{CO^5BOLD}$ model and the SME LTE model shows the largest deviation. The amplitude of the transmission curve is overpredicted within a factor of 2–3, and the difference to the IAG FTS results does not grow significantly larger than 1/1000.

The transmission curves are computed relative to the out-of-transit spectrum. This means that for the influence of CLV on the transmission curve, the relative differences between the line profiles observed at different limb positions are relevant while absolute differences between line profile calculations and the real profiles can be normalized out. The relative differences between line profiles at different limb positions in the IAG FTS Na I lines (upper left panel in Fig. 2) are more closely resembled by the $\mathrm{CO^5BOLD}$ calculations and the SME NLTE calculations than they are by the SME LTE calculations. This can explain why the $\mathrm{CO^5BOLD}$ and SME NLTE transmission curves are closer to the IAG FTS transmission curve than the SME LTE curve.
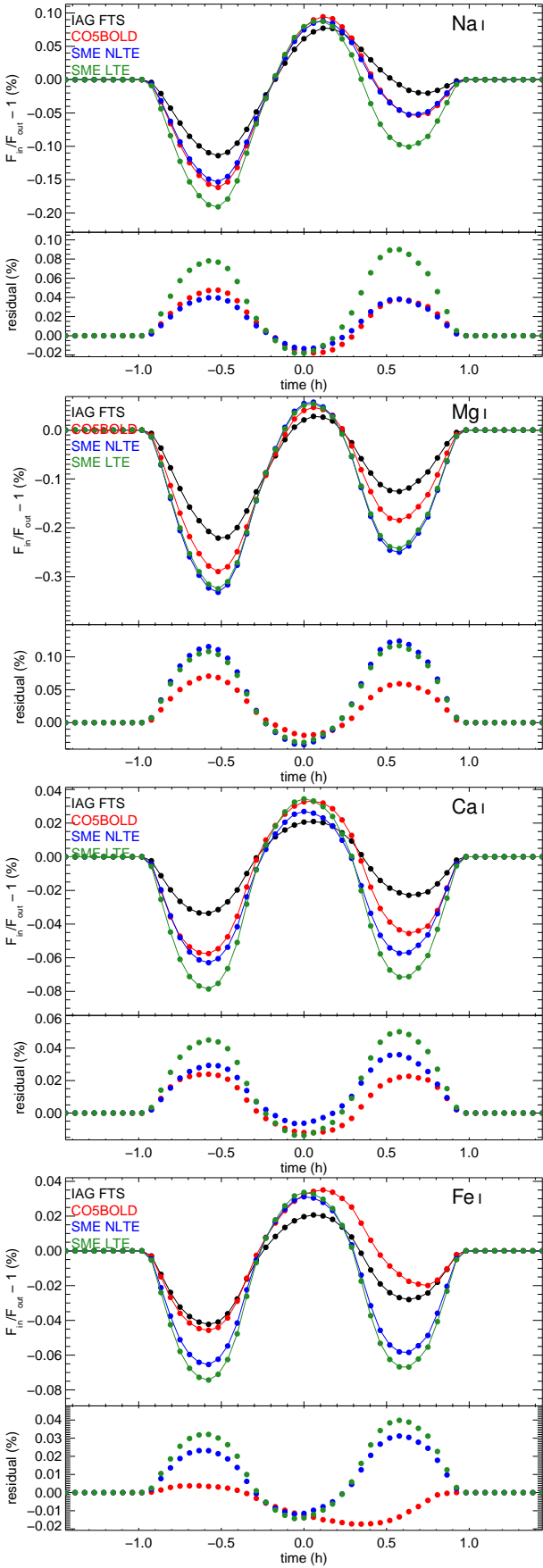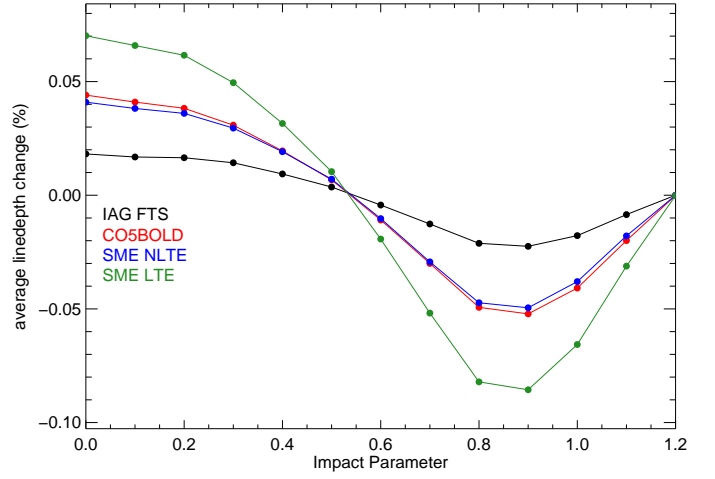
Fig. 5. Impact study showing the average line depth change for the Na I line depending on the impact parameter, a. The configuration is the same as in Table 2, but with orbital inclination according to the value of a.

Some of the transmission curves appear asymmetric. This is caused by asymmetries in the line profiles and their selective occultation during transit. Convective velocities can cause asymmetries in the observed IAG FTS line profiles and in the CO^5BOLD calculations. Their transmission curves show some asymmetry in all lines. For the SME calculations, no convection is taken into account. Nevertheless, SME transmission curves are also significantly asymmetric in the Na I and Mg I lines. This is because the line profiles of Na I and Mg I show some asymmetry that is caused by line blends, which is visible in the far wings of these lines (see Fig. 1). The Ca I and Fe I profiles, on the other hand, are rather symmetric. We note that normalization of the local line profiles can introduce systematic errors in the transmission curve, in particular if the lines extend to the edges of the integration region as in the Na I and Mg I examples. This can be relevant in transit observations because the continuum level may be difficult to determine.

We carry out an analysis of the difference between the transmission curve for the FTS IAG line profiles and the three model sets for a range of impact parameters, a. The impact parameter describes the minimum distance between the center of the star and the center of the planet during transit in units of the stellar radius; a transit occurs as long as $a < 1 + r_{planet}/r_{star}$ (grazing transits for $a > 1$). In Fig. 5, we show the average line depth change for impact parameters, a, between 0 and 1.2 for the case of the Na I line. We define the average line depth change as the integral of the transmission curve (top panel in Fig. 4) divided by the number of observations during transit. For impact parameters larger than $a \sim 0.55$, the average line depth is negative while it is positive for transits observed closer to the stellar center. This is because the Na I lines are deeper at disk center for all line profile sets (top panel in Fig. 1). Consistent with our result for the HD 189733b configuration ($a = 0.69$), the SME LTE profiles show the largest effect for all impact parameters. We conclude from Fig. 5 that the transmission curves computed from the three models scale with the transmission curve based on the FTS IAG profiles for all impact parameters.

Fig. 4. Example transmission curves and residuals between IAG FTS and model transmission curves for Na I, Mg I, Ca I, and Fe I (top to bottom). The configuration corresponds to the HD 189733b system (see Table 2).
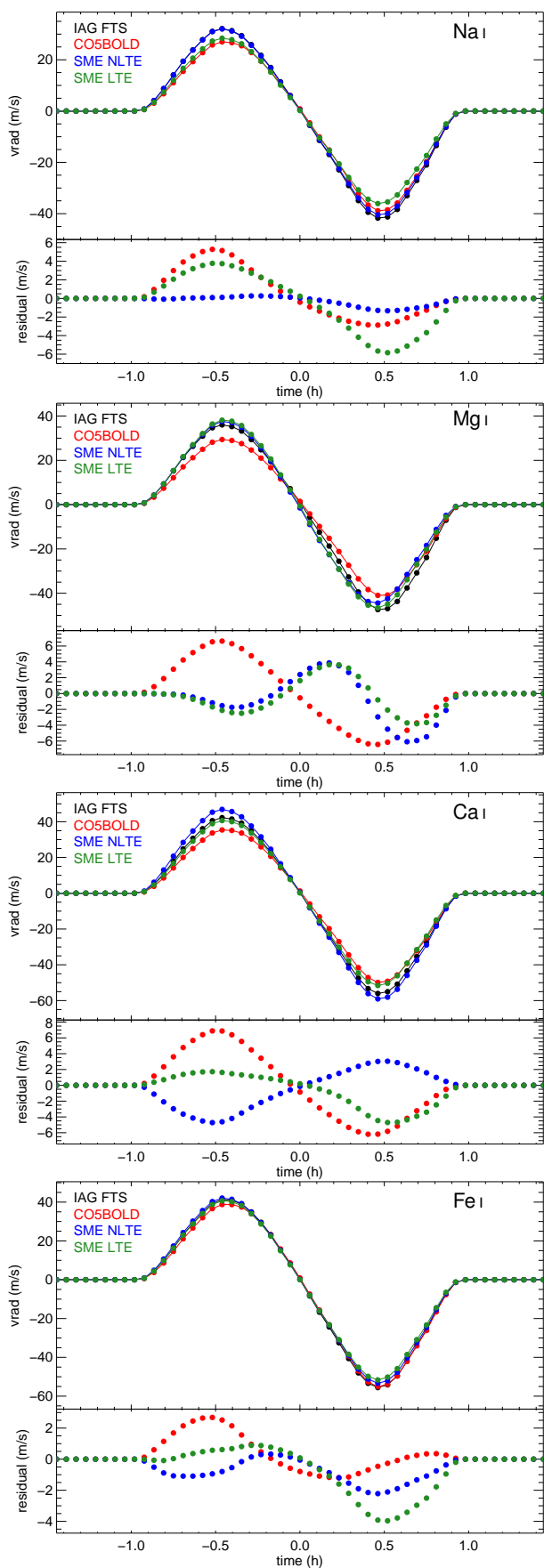
Fig. 6. Example RM curves and residuals between IAG FTS and model transmission curves for Na I, Mg I, Ca I, and Fe I (top to bottom). The configuration corresponds to the HD 189733b system (see Table 2).

4.2. Rossiter-McLaughlin curves

A wavelength dependence of planetary radius causes different amplitudes of the RM signal at different wavelengths, which is roughly proportional to the star's $v \sin i$ and the square of the planet-to-star radius ratio (Ohta et al. 2005). While this can be used to measure the planetary transmission spectrum (Snellen 2004; Dreizler et al. 2009), a chromatic RM effect can also be the result from chromatic CLV. The apparent variability of the line profile centroid during transit, visible in the RM curves, is shown for four spectral lines in Fig. 6. For each line, we simulated the disk-integrated line profiles with our observations of the solar surface and with the model line profiles from SME LTE, SME NLTE, and CO⁵BOLD. We computed the line center (the apparent radial velocity) by fitting a Gauss function to the cross-correlation between the disk-integrated spectra and the out-of-transit spectrum. Residuals between RM curves using solar observations and each of the model profiles are shown in the lower panel for each line.

The apparent radial velocities during transit depend on the shape of the line profiles, and also on the definition of line center for asymmetric lines. Here, we use the center of a Gauss fit to the cross-correlation between in- and out-of-transit spectra. In our examples, the overall shape of the RM curves are similar between the different spectral lines, but their amplitudes vary between ~60 m s⁻¹ in the Na I line and ~100 m s⁻¹ in the Fe I line. This is because the intrinsic line profiles and their CLV are different and therefore the occultation of the stellar surface at the same projected local velocity leads to different line profile deformations in different spectral lines.

In general, the four versions of local line profiles lead to consistent RM curves for each of the four spectral lines, albeit the CO⁵BOLD profiles tend to show an amplitude up to 10 m s⁻¹ weaker than the other three sets of profiles. The SME LTE and NLTE calculations lead to relatively similar outcomes, especially for the Mg I and the Fe I lines. The deviations between the RM curves computed with IAG FTS profiles and those from the simulations show no preferred pattern of symmetry, except for the CO⁵BOLD case in which the RM curve is always underestimated before midtransit. This is likely caused by the overpredicted blue wing of the CO⁵BOLD calculations (see Section 3.4). During the first half of the transit, the planet occults the blueshifted areas of the rotating stellar surface, which leads to a smaller RM amplitude if the blue wing is broader. We find that for the HD 189733 configuration, the uncertainty in the RM curve due to unknown CLV is on the order of a few m s⁻¹ and always smaller than 10 m s⁻¹.

We investigate the mismatch between RM curves from the model line profiles and the observed solar CLV for different transit configurations in an impact parameter study. In Fig. 7, we show the average deviation (with the same definition as for the average transmission curve in Section 4.1) during transit between model and solar CLV for the three models as a funcion of the impact parameter for the Na I line. As expected from the HD 189733b simulation shown in the top panel of Fig. 6, the SME NLTE profiles show the smallest deviation from the solar CLV case, but this would be different for other lines. The mismatch tends to to be larger when the transit happens closer to the stellar center and reaches average values exceeding 3 m s⁻¹.

5. Summary and discussion

We present a detailed investigation of CLV observed in the solar library from Ellwarth et al. (2023). We focus on four spectral
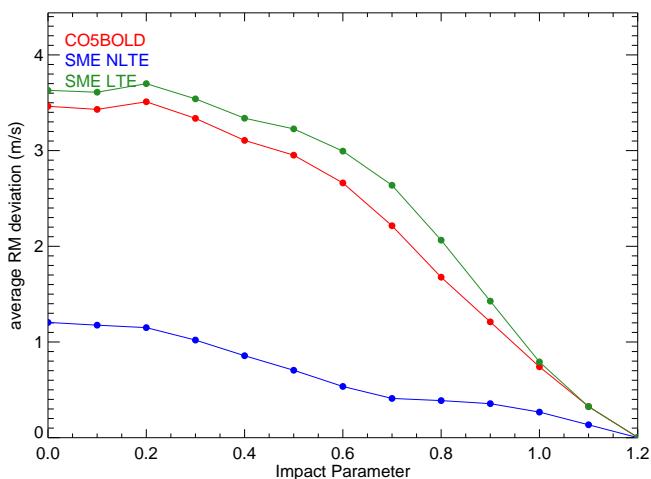
Fig. 7. Impact study showing average RM deviation change for the Na I line depending on the impact parameter, a. The configuration is the same as in Table 2, but with orbital inclination according to the value of a.

lines in the visible wavelength range from four different ions: Na I, Mg I, Ca I, and Fe I. We compare the line shape and CLV to three different spectral models. Our first synthetic spectrum was computed under the assumption of LTE and without convection (SME LTE), the second included NLTE effects but no convection (SME NLTE), and the third included 3D convection but line formation is based on LTE (CO^5BOLD). Our goal was to separate the effects of NLTE and convection on spectral line formation and CLV, and to estimate to which extent the models can reproduce the behavior of spectral lines.

In most cases, the line depths are best matched by the NLTE model with the exception of Mg I. The LTE models typically produce lines that are weaker than the observations, and the CLV is generally overestimated by the models. All four example lines are relatively strong with core transmission being less than 20 %. They show little CLV in the line cores but strong differences with limb position in the wings of the lines where CLV is relatively better predicted by the models. For the Na I line, neglecting NLTE effects produces a particularly large difference between the model and observations.

The observed spectral lines are asymmetric, and their shape varies with limb position. Lines from 1D models are symmetric by design and therefore cannot reproduce line asymmetries and their limb effect. The CO^5BOLD calculations appear more asymmetric than the observation, and they tend to overpredict the blue wings of the line profiles. The relative variability of the line shape with limb position predicted by the CO^5BOLD model shows trends similar to the observed CLV, but its variability comes out stronger than observed. Qualitatively, the best match is achieved for the Fe I line, in which NLTE effects are negligible and the CO^5BOLD model reproduces the observations relatively well.

We show simulations of spectral lines during planetary transits and investigate the impact of CLV on the planetary trace caused by occultation only, that is, the RM effect, for a Sun-like star. This is relevant for understanding the influence of CLV on the detectability of planetary atmospheres. We find that narrow-band transmission curves are typically overestimated by any of the three models; predictions of transit depth are up to a factor of two larger than the ones computed with the observed line profiles. In the RM curves, the models predict amplitudes that can

be lower or larger in amplitude than the curves based on solar observations. The maximum deviations we found for a transit with a configuration similar to HD 189733b are roughly 5 m s^{-1} for the Na I line. Peak amplitude differences are on the order of 5–10 m s^{-1}, but they could be larger for other lines and configurations, and in different stars. This can easily exceed the chromatic RM expected from the presence of atoms such as Na in the atmosphere of a planet (Snellen 2004; Di Gloria et al. 2015; Oshagh et al. 2020).

We conclude that neither of the three models provides a representative prediction of any of the four strong lines used in our examples. This is not surprising because the model spectra we used were not optimized to match the observed line profiles. The solar observations provide important information for atmospheric and convection models. Our simulations of transmission curves can be used to estimate the uncertainty in analyses of exoplanet atmosphere spectra for spectral lines that appear in the stellar spectrum. For Sun-like stars, models seem to overpredict the signature of the planetary trace that occurs in the absence of a planetary atmosphere. Extrapolations to stars different than the Sun are not straightforward because line formation processes can be very different in their atmospheres. We provide data and models used here to allow simulations of planetary transits in the spectral lines contained in the data.

References

Amarsi, A. M., Lind, K., Asplund, M., Barklem, P. S., & Collet, R. 2016, MNRAS, 463, 1518
Amarsi, A. M., Lind, K., Osorio, Y., et al. 2020, A&A, 642, A62
Asplund, M., Grevesse, N., Sauval, A. J., & Scott, P. 2009, A&A Rev., 47, 481
Athay, R. G., Lites, B. W., White, O. R., & Brault, J. W. 1972, Sol.Phys., 24, 18
Balthasar, H. 1984, Sol.Phys., 93, 219
Beckers, J. M. & Nelson, G. D. 1978, Sol.Phys., 58, 243
Caffau, E., Ludwig, H. G., Steffen, M., Freytag, B., & Bonifacio, P. 2011, Sol. Phys., 268, 255
Casasayas-Barris, N., Palle, E., Stangret, M., et al. 2021, A&A, 647, A26
Casasayas-Barris, N., Pallé, E., Yan, F., et al. 2020, A&A, 635, A206
Cavallini, F., Ceppatelli, G., & Righini, A. 1985, A&A, 150, 256
Chiavassa, A. & Brogi, M. 2019, A&A, 631, A100
Csizmadia, S., Pasternacki, T., Dreyer, C., et al. 2013, A&A, 549, A9
Czesla, S., Klocová, T., Khalafinejad, S., Wolter, U., & Schmitt, J. H. M. M. 2015, A&A, 582, A51
Di Gloria, E., Snellen, I. A. G., & Albrecht, S. 2015, A&A, 580, A84
Dravins, D., Lindegren, L., & Nordlund, A. 1981, A&A, 96, 345
Dravins, D., Ludwig, H.-G., Dahlén, E., & Pazira, H. 2017a, A&A, 605, A90
Dravins, D., Ludwig, H.-G., Dahlén, E., & Pazira, H. 2017b, A&A, 605, A91
Dravins, D., Ludwig, H.-G., & Freytag, B. 2021, A&A, 649, A17
Dreizler, S., Reiners, A., Homeier, D., & Noll, M. 2009, A&A, 499, 615
Dumusque, X., Boisse, I., & Santos, N. C. 2014, ApJ, 796, 132
Ellwarth, M., Schäfer, S., Reiners, A., & Zechmeister, M. 2023, A&A, accepted for publication
Espinoza, N. & Jordán, A. 2015, MNRAS, 450, 1879
Freytag, B., Steffen, M., Ludwig, H. G., et al. 2012, Journal of Computational Physics, 231, 919
González Hernández, J. I., Rebolo, R., Pasquini, L., et al. 2020, A&A, 643, A146
Grevesse, N., Asplund, M., & Sauval, A. J. 2007, Space Sci. Rev., 130, 105
Gustafsson, B., Edvardsson, B., Eriksson, K., et al. 2008, A&A, 486, 951
Haywood, R. D., Collier Cameron, A., Unruh, Y. C., et al. 2016, MNRAS, 457, 3637
Hubeny, I. & Lanz, T. 2011, TLUSTY: Stellar Atmospheres, Accretion Disks, and Spectroscopic Diagnostics, Astrophysics Source Code Library, record ascl:1109.021
Huke, P., Debus, M., Zechmeister, M., & Reiners, A. 2019, J. Opt. Soc. Am. B, 36, 1899
Koesterke, L. 2009, in American Institute of Physics Conference Series, Vol. 1171, Recent Directions in Astrophysical Quantitative Spectroscopy and Radiation Hydrodynamics, ed. I. Hubeny, J. M. Stone, K. MacGregor, & K. Werner, 73–84

Koesterke, L., Allende Prieto, C., & Lambert, D. L. 2008, ApJ, 680, 764

Kupka, F., Piskunov, N., Ryabchikova, T. A., Stempels, H. C., & Weiss, W. W. 1999, A&AS, 138, 119

Lagrange, A.-M., Desort, M., & Meunier, N. 2010, A&A, 512, A38

Lanza, A. F., Bonomo, A. S., Moutou, C., et al. 2010, A&A, 520, A53

Lee, D. T. & Schachter, B. J. 1980, International Journal of Computer & Information Sciences, 9, 219

Livingston, W. C. 1982, Nature, 297, 208

Ludwig, H. G., Caffau, E., Steffen, M., et al. 2009, Mem. Soc. Astron. Italiana, 80, 711

Marchwinski, R. C., Mahadevan, S., Robertson, P., Ramsey, L., & Harder, J. 2015, ApJ, 798, 63

Maxted, P. F. L. & Gill, S. 2019, A&A, 622, A33

Meunier, N., Desort, M., & Lagrange, A.-M. 2010a, A&A, 512, A39

Meunier, N., Lagrange, A.-M., & Desort, M. 2010b, A&A, 519, A66

Milbourne, T. W., Haywood, R. D., Phillips, D. F., et al. 2019, ApJ, 874, 107

Neckel, H. & Labs, D. 1994, Sol. Phys., 153, 91

Nordlund, Å., Stein, R. F., & Asplund, M. 2009, Living Reviews in Solar Physics, 6, 2

Ohta, Y., Taruya, A., & Suto, Y. 2005, ApJ, 622, 1118

Oshagh, M., Bauer, F. F., Lafarga, M., et al. 2020, A&A, 643, A64

Parviainen, H. & Aigrain, S. 2015, MNRAS, 453, 3821

Piskunov, N. & Valenti, J. A. 2017, A&A, 597, A16

Piskunov, N. E., Kupka, F., Ryabchikova, T. A., Weiss, W. W., & Jeffery, C. S. 1995, A&AS, 112, 525

Reiners, A., Lemke, U., Bauer, F., Beeck, B., & Huke, P. 2016a, A&A, 595, A26

Reiners, A., Mrotzek, N., Lemke, U., Hinrichs, J., & Reinsch, K. 2016b, A&A, 587, A65

Schäfer, S., Huke, P., Meyer, D., & Reiners, A. 2020a, in Society of Photo-Optical Instrumentation Engineers (SPIE) Conference Series, Vol. 11447, Society of Photo-Optical Instrumentation Engineers (SPIE) Conference Series, 114473Q

Schäfer, S., Royen, K., Huster Zapke, A., Ellwarth, M., & Reiners, A. 2020b, in Society of Photo-Optical Instrumentation Engineers (SPIE) Conference Series, Vol. 11447, Society of Photo-Optical Instrumentation Engineers (SPIE) Conference Series, 11447A9

Snellen, I. A. G. 2004, MNRAS, 353, L1

Steffen, M., Prakapavičius, D., Caffau, E., et al. 2015, A&A, 583, A57

Stenflo, J. O. 2015, A&A, 573, A74

Tremblay, P. E., Ludwig, H. G., Freytag, B., Steffen, M., & Caffau, E. 2013, A&A, 557, A7

Triaud, A. H. M. J., Queloz, D., Bouchy, F., et al. 2009, A&A, 506, 377

Valenti, J. A. & Piskunov, N. 1996, A&AS, 118, 595

Yan, F., Fosbury, R. A. E., Petr-Gotzens, M. G., Zhao, G., & Pallé, E. 2015, A&A, 574, A94

Yan, F., Pallé, E., Fosbury, R. A. E., Petr-Gotzens, M. G., & Henning, T. 2017, A&A, 603, A73

Appendix A: Abundances used in the synthetic spectrum calculations

Table A.1. Chemical abundances used in the computation of the SME spectra and the synthetic 3D spectrum based on the CO^5BOLD model atmosphere.

Z	X	log A(X)		Z	X	log A(X)	
		SME	CO^5BOLD			SME	CO^5BOLD
1	H	12.00	12.00	44	Ru	1.84	1.84
2	He	10.93	10.93	45	Rh	1.12	1.12
3	Li	1.05	1.10	46	Pd	1.66	1.69
4	Be	1.38	1.40	47	Ag	0.94	0.94
5	B	2.70	2.55	48	Cd	1.77	1.77
6	C	8.39	8.52	49	In	1.60	1.66
7	N	7.78	7.92	50	Sn	2.00	2.00
8	O	8.66	8.83	51	Sb	1.00	1.00
9	F	4.56	4.56	52	Te	2.19	2.24
10	Ne	7.84	8.08	53	I	1.51	1.51
11	Na	6.17	6.33	54	Xe	2.24	2.17
12	Mg	7.53	7.58	55	Cs	1.07	1.13
13	Al	6.37	6.47	56	Ba	2.17	2.13
14	Si	7.51	7.55	57	La	1.13	1.17
15	P	5.36	5.45	58	Ce	1.70	1.58
16	S	7.14	7.33	59	Pr	0.58	0.71
17	Cl	5.50	5.50	60	Nd	1.45	1.50
18	Ar	6.18	6.40	62	Sm	1.00	1.01
19	K	5.08	5.12	63	Eu	0.52	0.51
20	Ca	6.31	6.36	64	Gd	1.11	1.12
21	Sc	3.17	3.17	65	Tb	0.28	−0.10
22	Ti	4.90	5.02	66	Dy	1.14	1.14
23	V	4.00	4.00	67	Ho	0.51	0.26
24	Cr	5.64	5.67	68	Er	0.93	0.93
25	Mn	5.39	5.39	69	Tm	0.00	0.00
26	Fe	7.45	7.50	70	Yb	1.08	1.08
27	Co	4.92	4.92	71	Lu	0.06	0.06
28	Ni	6.23	6.25	72	Hf	0.88	0.88
29	Cu	4.21	4.21	73	Ta	−0.17	−0.13
30	Zn	4.60	4.60	74	W	1.11	1.11
31	Ga	2.88	2.88	75	Re	0.23	0.28
32	Ge	3.58	3.41	76	Os	1.25	1.45
33	As	2.29	2.37	77	Ir	1.38	1.35
34	Se	3.33	3.41	78	Pt	1.64	1.80
35	Br	2.56	2.63	79	Au	1.01	1.01
36	Kr	3.25	3.31	80	Hg	1.13	1.13
37	Rb	2.60	2.60	81	Tl	0.90	0.90
38	Sr	2.92	2.97	82	Pb	2.00	1.95
39	Y	2.21	2.24	83	Bi	0.65	0.71
40	Zr	2.58	2.60	90	Th	0.06	0.09
41	Nb	1.42	1.42	92	U	−0.52	−0.50
42	Mo	1.92	1.92				